ChemComm

COMMUNICATION

View Article Online
View Journal | View Issue

Cite this: *Chem. Commun.*, 2016, 52, 9141

Received 14th March 2016,
Accepted 20th April 2016

DOI: 10.1039/c6cc02252a

www.rsc.org/chemcomm

Small-pore driven high capacitance in a hierarchical carbon *via* carbonization of Ni-MOF-74 at low temperatures†

J. A. Carrasco,‡[a] J. Romero,‡[a] G. Abellán,[b] J. Hernández-Saz,[c] S. I. Molina,[c] C. Martí-Gastaldo*[a] and E. Coronado[a]

A hierarchical porous carbon prepared *via* direct carbonization of Ni-MOF-74 loaded with furfuryl alcohol at 450 °C displays high specific capacitance in comparison with other MOF-derived carbons as a result of the formation of micropores smaller than 1 nm.

Research in Metal–Organic Frameworks (MOFs) has primarily targeted application in storage and separation technologies,[1] catalysis[2] or sensing[3] to cite a few. It is more recently that the thermal stability, internal voids and unique structural/chemical flexibility of MOFs have been used to produce porous, nanostructured materials by direct calcination. This strategy is similar to the nanocasting method,[4] traditionally used for producing hierarchical porous carbons by pyrolysis of mesoporous hosts filled with carbon precursors followed by removal of the inorganic template. In comparison with mesoporous inorganic solids, that are restricted to act as sacrificial templates, MOFs offer higher synthetic flexibility. Their hybrid organic/inorganic nature allows for producing nanoporous carbons by direct decomposition of the organic linkers in their structure with no need for auxiliary carbon sources.[5] MOFs also feature smaller pore metrics (microporosity) and easy modification of the organic linkers for variable pore wall chemistry.

Nanocasting of ZIF-8,[6] Al-PCP[7] or MOF-5[8] with furfuryl alcohol (FA) or urea acting as auxiliary carbon sources has been used to produce nanoporous carbons with a variable surface area and electrochemical activity of interest in hydrogen storage and electric double-layer capacitors (EDLCs). This route has been mainly limited to Zn(II) templates due to the easy removal of the metal by evaporation during heat treatment. The use of alternative MOF templates that incorporate metal centres like Fe, Co and Ni, capable of catalysing the carbon decomposition, is worth being explored. This would also endow carbon porous nanocomposites with the metal components required to access environmentally relevant applications like electrocatalysis, supercapacitors and water remediation.[9]

In this context, Ni-MOF-74[10] is a promising candidate that still remains to be explored. It combines a long-range ordered array of Ni(II) catalytic centres with a surface area close to 1000 $m^2\ g^{-1}$ (*cf.* 1370 for ZIF-8) featuring a honeycomb distribution of 1D channels with a pore diameter of 11 Å, big enough to accommodate FA molecules. MOF-74 is a family of isostructural compounds formulated as $M_2(dhtp)(H_2O)_2$ (M = Mg, Mn, Fe, Co, Ni, and Zn; dhtp = 2,5-dihydroxyterephthalate).[11,12] Thus, the catalytic activity of the template can be finely tuned by a suitable choice of the metal, or combination of metals, in the porous scaffold to control the crystallinity and porosity of the resulting carbon. Furthermore, previous reports suggest a linear correlation between the M/C ratio in zinc MOFs acting as sacrificial precursors and the surface area of the resulting carbons.[13] Carbon poor organic linkers might be thus better fitted to produce a bigger number of metal particles, which can be then removed for overall increase in porosity. Ni-MOF-74 features a ratio of 0.25, well above those displayed by Al-PCP, Fe-BTC, ZIF-8, MOF-5, MIL-100 or HKUST-1 between 0.08 and 0.17. A delicate control over these features is the key to maximizing the performance of MOF-derived carbons as electrodes in EDLCs.

Ni-MOF-74 was prepared by a solvothermal reaction of $Ni(NO_3)_2$ and dhtp and pre-treated at reduced pressure for solvent removal. The activated solid was then soaked in furfuryl alcohol. The mixture was heated at 60 °C for 12 hours with soft stirring for favouring the diffusion of FA into the pores of the MOF, followed by thorough washing with ethanol to remove non-infiltrated FA molecules stuck to the surface of the crystals (synthetic details in SI2, ESI†). The phase purity and morphology of Ni-MOF-74/FA was studied using powder X-ray diffraction (PXRD) and Scanning Electron Microscopy (SEM) to rule out structural changes upon solvent removal or guest loading (Fig. SI3 and SI4, ESI†). The solid is isolated as yellowish, micrometric crystals featuring a rose-like morphology. Indexing of the PXRD pattern agrees well with a pure MOF-74 phase.

[a] *Instituto de Ciencia Molecular, Universitat de València, Catedrático José Beltrán 2, 46980, Paterna, Spain. E-mail: carlos.marti@uv.es*
[b] *Department of Chemistry and Pharmacy and Joint Institute of Advanced Materials and Processes (ZMP), University Erlangen-Nürnberg, Henkestr. 42, 91054 Erlangen and Dr.-Mack Str. 81, 90762 Fürth, Germany*
[c] *Departamento de Ciencia de los Materiales e I.M. y Q.I., Facultad de Ciencias, IMEYMAT, Universidad de Cádiz, Campus Río San Pedro, s/n, 11510, Cádiz, Spain*
† Electronic supplementary information (ESI) available. See DOI: 10.1039/c6cc02252a
‡ JAC and JR contributed equally to this work.

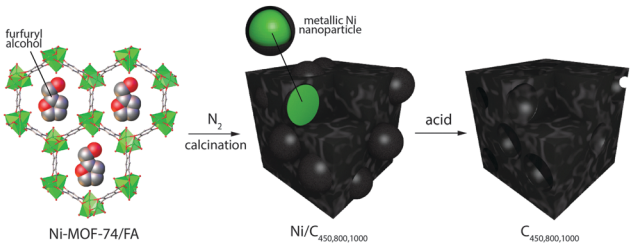

Fig. 1 Synthetic route for producing Ni/C composites and hierarchical carbons.

Complete filling of the pores with FA is consistent with the drastic reduction of the Brunauer–Emmett–Teller (BET) surface area (N_2, 77 K): from 883.1 for the activated solid to 4.1 m^2 g^{-1} in Ni-MOF-74/FA (Fig. SI5, ESI†). Thermogravimetric analysis reveals that the FA content oscillates around 0.5 molecules per MOF unit formula, representing close to 25% of the total carbon content in the composite (Fig. SI6, ESI†).

Ni-MOF-74/FA was charged in a quartz vessel and transferred to a tubular furnace. The solid was first heated at 250 °C under a flow of N_2. This temperature remains below the thermal stability of the MOF so this step was used to produce Ni-MOF-74/C_{250} by polymerization of FA. In line with previous reports,[7] this process shall be favoured by the presence of multiple –OH groups from dhtp that are known to act as catalytic Brönsted acid sites for FA polymerization. Next, Ni-MOF-74/C_{250} was carbonized in N_2 at 450, 800 and 1000 °C to produce Ni/C_{450}, Ni/C_{800} and Ni/C_{1000} (Fig. 1). In this step both, polymerized FA and the organic linker in the MOF scaffold, undergo decomposition/carbonization catalysed by the presence of Ni centres to produce the corresponding carbons. Thermal-driven transformation was monitored by studying the evolution of the PXRD of these solids (Fig. 2a). Ni-MOF-74/C_{250} retains the original structure of the pristine MOF and displays negligible porosity (Fig. SI8, ESI†). This agrees well with the formation of amorphous carbon from FA polymerization that occupies the 1D channels deployed by the MOF. In turn, carbonization at 450 °C prompts the disappearance of the PXRD fingerprint of Ni-MOF74 to give rise to two broad shoulders at 44.5 and 51.8°. This supports the collapse of the structure of the MOF linked to its decomposition and the incipient formation of metallic Ni in Ni/C_{450}. Ni/C_{800} and Ni/C_{1000} display almost identical PXRDs dominated by much sharper, intense diffraction lines associated with metallic Ni along with a broad shoulder centered at 26.2° (3.39 Å), that agrees well with the position of (001) in graphite (d_{001} = 3.36 Å). This suggests that the formation of crystalline Ni clusters in the composite might facilitate the formation of more crystalline carbon at higher temperatures. The original rose-like morphology of Ni-MOF-74 is retained for all composites according to their SEM images (Fig. 2b and Fig. SI9, ESI†). This confirms that carbon formation takes place in the interior of the MOF crystals rather than from FA molecules adsorbed on their surface. The only difference in the texture of the crystals linked to calcination temperature is the appearance of protuberances in the facets of the crystals in Ni/C_{800} that become more abundant at higher temperatures for Ni/C_{1000}. The internal structure of the composites was studied *via* cross-section imaging using Focused Ion Beam-Scanning Electron Microscopy (FIB-SEM).

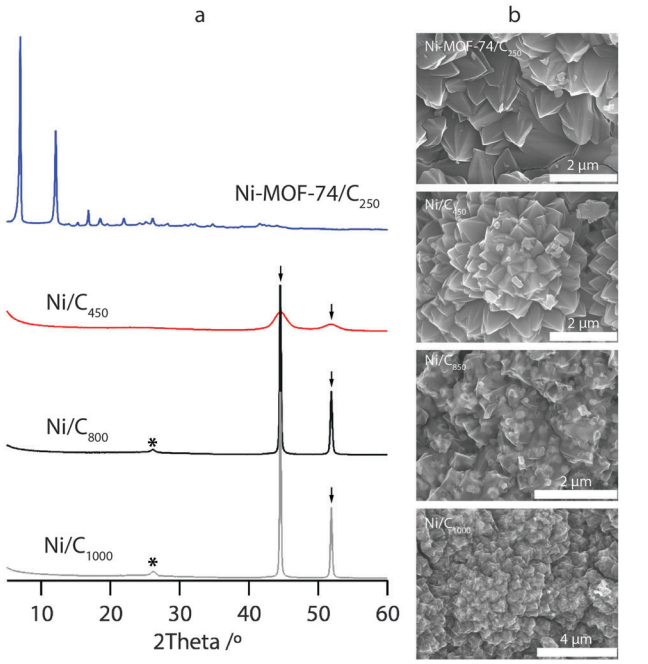

Fig. 2 PXRD (a) and SEM images (b) of –from top to bottom– Ni-MOF-74/C_{250}, Ni/C_{450}, Ni/C_{800} and Ni/C_{1000}. Diffraction lines indexed to Ni (ICDD-JCPDS Card No. 04-0850) are indicated with arrows. The shoulder associated with the formation of a graphitic carbon is indicated with an asterisk.

As shown in Fig. 3a, Ni/C_{450} displays flat sections with homogeneous contrast and sub-micrometric cracks, likely originated from the mechanical strain linked to the initial stages of carbon decomposition. Cross-sections of Ni/C_{800} (Fig. 3b) and Ni/C_{1000} (Fig. 3c) feature more irregular sections with a homogeneous distribution of brighter holes, quite close in size, reminiscent of the protuberances identified in the outer surface of the crystals. These internal pores are probably generated by more quantitative release of internally generated gases like CO and CO_2 upon calcination at higher temperatures.[14]

High-Resolution Transmission Electron Microscopy (HR-TEM; Fig. 3d) was used to confirm the formation of Ni nanoparticles encapsulated within a carbonaceous matrix. Selected-area electron diffraction (SAED) patterns acquired from a region of 250 nm display several rings, which can be indexed as the characteristics (111), (200) and (220) diffraction planes of Ni fcc. TEM was used to correlate the size of the NPs with the calcination temperature. Our study confirms that C/Ni_{450} displays the smallest size (7 nm) that increases up to 100 nm for 800 and 1000 °C (Fig. SI11, ESI†) as the result of more favourable mass diffusion at higher temperatures. The Ni formation is consistent with the room temperature magnetism shown by all composites. For example, Ni/C_{1000} behaves as a soft ferromagnet with a value of the magnetization at the saturation of 31.3 emu g^{-1} at 300 K (Fig. SI12, ESI†). This is slightly below that reported for Ni NPs of similar size, suggesting partial surface oxidation.[15] The formation of defective, graphitic carbon was confirmed by the presence of characteristic G and D bands in the Raman spectra (Fig. SI13, ESI†). The intensity ratio of I_G/I_D remains close to one (Table SI13, ESI†), with values similar to those reported for carbons prepared *via* carbonization of MOFs like

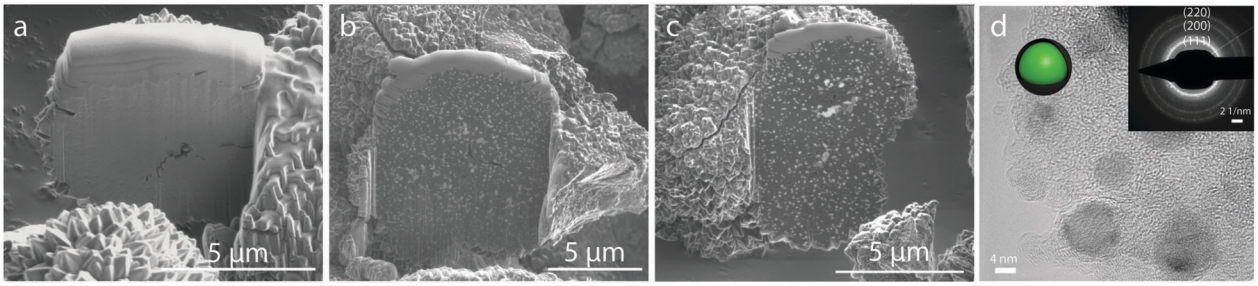

Fig. 3 FIB-SEM images of the cross section of Ni/C_{450} (a), Ni/C_{800} (b) and Ni/C_{1000} (c). See SI10 (ESI†) for images of additional sections for each sample. (d) HR-TEM image of C/Ni_{450}. Inset shows SAED pattern highlighting characteristic diffraction rings of Ni fcc.

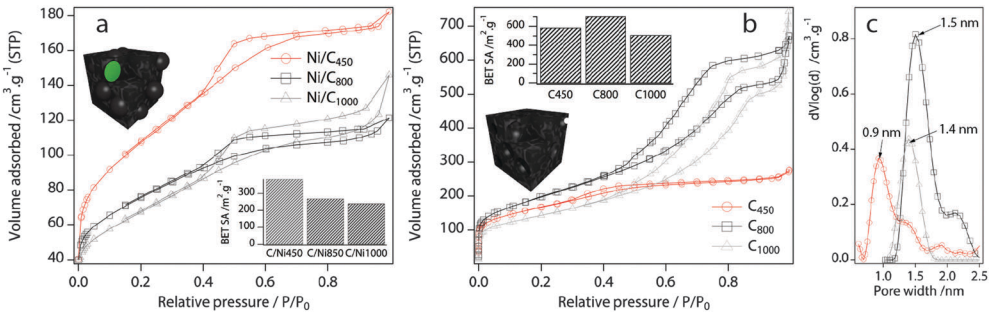

Fig. 4 N_2 isotherms and BET surface areas for Ni/C composites (a) and derived carbons (b). (c) Pore size distribution in metal-free carbons. See Tables SI14 and SI17 (ESI†) for complete porosity metrics.

ZIF-8,[5] MOF-5 or IRMOF-3.[16] The 2D band is present only for Ni/C_{800} and Ni/C_{1000}, confirming the formation of more graphitized, crystalline carbon at higher temperatures as anticipated using PXRD (Fig. 2).

Porosity was studied by N_2 adsorption–desorption measurements at 77 K (Fig. 4). Composites display combined I/IV isotherms with a hysteresis loop at $0.4 < P/P_0 < 0.99$, characteristic of the combination of micro- and mesoporosity. Pore size distribution (PSD) was analysed by quenched solid density functional theory (QSDFT; SI14, ESI†), indicating a combination of micropores close to 2.0 nm with well-defined mesopores centered at around 4 nm. Compared with pristine Ni-MOF-74, there is a drastic reduction of BET surface area that becomes smaller at higher calcination temperatures as a result of structural collapse. Still, Ni/C_{450} displays significant porosity with the highest BET of the series of 383 $m^2\ g^{-1}$ and a micropore volume of 0.143 $cm^3\ g^{-1}$ (30% of the original value). Metal NPs were dissolved by soaking the composite in HNO_3 (aq) at 80 °C and confirmed by electron probe microanalysis after acid treatment (Fig. SI15, ESI†). All carbons display higher BETs than their metal composite counterparts with total pore volumes close to 0.8 for C_{800} and C_{1000} and 0.4 $cm^3\ g^{-1}$ for C_{450}. Though the original MOF structure cannot be retained upon thermal treatment, it plays a templating role for evenly distributing Ni NPs in a 3D meso/microporous carbon network and transferring hierarchical porosity to the resulting carbon. In fact all carbons retain a considerable fraction of micropore volume after metal leaching that reaches a maximum of 50% of the total for C_{450}. The PSD confirms the presence of hierarchical porosity in all carbons. The distribution is comparatively narrow for C_{450} that features well-defined micropores centered at 0.9 nm whilst the width of the distribution and the average pore size increases up to 1.5 nm at higher temperatures (Fig. 4 and Fig. SI17, ESI†).

MOF-derived carbons have proven to be quite promising for energy storage applications when used as electrodes in EDLCs.[9] We tested the electrochemical performance of Ni-MOF-74 derived carbons in a conventional three-electrode cell in 6 M KOH aqueous electrolyte in a voltage window of −1 to 0 V (*vs.* Ag/AgCl). Fig. 5a shows cyclic voltammograms (CVs) of carbons at 100 mV s^{-1}. Deviation from the rectangle-like shape characteristic of carbon EDLCs is more drastic at higher speeds and more pronounced for C_{450} as a result of the presence of smaller micropores that limit electrolyte diffusion rates at shorter transport times. The CV of C_{450} also features a bump indicative of a pseudocapacitive contribution to the overall capacitive response associated with the presence of oxygen-doped carbon atoms. This is consistent with its high-resolution O 1s XPS spectrum that can be fitted to two components centered at 531.7 and 533.2 eV, which correspond to C═O and C–O groups (Fig. SI19, ESI†). O-doping results from carbonization at low temperature of $–CO_2H$ and –OH groups in dhtp and loaded FA for a total atomic % of 13.4. Capacitance was evaluated by measuring galvanostatic discharge curves at variable current densities that display a slightly curved profile also due to O-doping, which becomes less pronounced for higher calcination temperatures (Fig. 5b, see Fig. SI18, ESI† for the complete electrochemical study). Fig. 5b shows the evolution of specific capacitance for the family of carbons, calculated by integrating the discharge curve with the discharge current. Specific capacitance decreases with increasing calcination

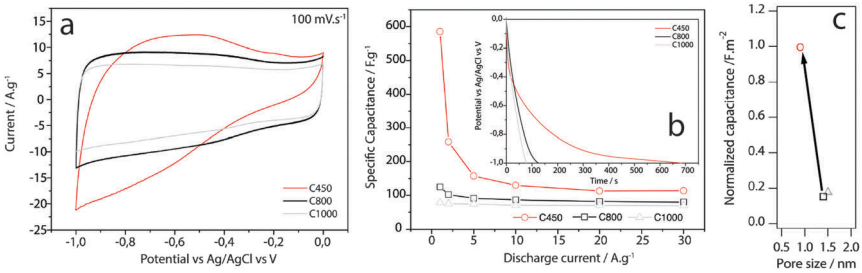

Fig. 5 Electrochemical properties of carbons. (a) CVs at 100 mV s^{-1} in a 6 M KOH (aq) electrolyte. (b) Evolution of specific capacitance with discharge current. Inset shows galvanostatic discharge curves at 1 A g^{-1}. (c) Evolution of capacitance normalized to the surface area with average pore size extracted from N_2 isotherms.

temperature with C_{450} displaying the maximum capacity of 585 F g^{-1} at 1 A g^{-1}, that stands among the highest capacitance reported for a MOF-derived carbon to date (Table SI17, ESI†). Contrary to the common belief that stands for a concomitant increase of capacitance with the surface area, SA of C_{450} (587 m^2 g^{-1}) is below that of C_{800} (*ca.* 706), from the same family, or values as high as 2169 m^2 g^{-1} for carbons prepared from ZIF-8[17] but displays higher capacitance. Aside from O-doping, we ascribe this abnormal increase in capacitance to the presence of micropores of small size, which have been reported to be very effective in favouring ionic transport for the total increase of double-layer capacitance in carbons.[18] This effect agrees well with the variation of specific capacitance normalized to SA with the pore size, that reveals a dramatic increase for C_{450} (Fig. 5c). Small-size micropores are hard to evaluate with N_2 due to diffusion limitations. Hence, we used CO_2 adsorption at 273 K to further confirm the presence of pores <0.7 nm (Fig. SI16, ESI†). According to our results, these are responsible for 70% of the microporosity of C_{450} whilst their contribution to overall porosity decreases down to 40% for carbons produced at higher temperatures (Table SI17, ESI†). PXRD (Fig. 2a), Raman (Fig. SI13, ESI†) and HR-TEM (Fig. SI22, ESI†) also confirm that C_{450} is mainly amorphous in nature whilst higher temperatures induce partial graphitization. In line with recent reports for NiO, specific capacitance from bulk contribution is expected to be higher for amorphous electrodes than for crystalline ones due to shorter diffusion path lengths for the electrolyte to cover.[19] C_{450} displays a capacity retention close to 80% after 10.000 charge–discharge cycles (Fig. S21, ESI†).

The use of MOF incorporation of catalytically active metals as sacrificial templates for the carbon synthesis endows control over the crystallinity, degree of graphitization and textural properties of the resulting carbon with the calcination temperature. In contrast to previous reports reliant on MOFs based on inert metals, the introduction of Ni enables the formation of oxygen-doped, amorphous carbon to take place at comparatively low temperatures (450 °C). Lower calcination temperatures also allow for the formation of a hierarchical carbon with micropores smaller than 1 nm. This translates into a drastic increase in gravimetric capacitance, among the highest reported for MOF-derived carbons to date. Whereas a sufficient surface area is the key to maximise electrode/electrolyte contact, our work suggests that temperature control over pore size distribution might be more effective in leading to carbons with a superior charge storage.

This work was supported by the Spanish MINECO (Project MAT-2014-56143-R and the Unit of Excellence María de Maeztu MDM-2015-0538) and the Generalitat Valenciana (Prometeo). J. A. C. and J. R. thank the Universidad de Valencia for a pre-doctoral grant. G. A. thanks the EU for a Marie Curie Fellowship (FP7/2013-IEF-627386). C. M.-G. thanks the Spanish MINECO for a Ramón y Cajal Fellowship.

Notes and references

1 B. Van de Voorde, B. Bueken, J. Denayer and D. De Vos, *Chem. Soc. Rev.*, 2014, **43**, 5766–5788.
2 J. Gascon, A. Corma, F. Kapteijn and F. X. Llabrés i Xamena, *ACS Catal.*, 2014, **4**, 361–378.
3 L. E. Kreno, K. Leong, O. K. Farha, M. Allendorf, R. P. Van Duyne and J. T. Hupp, *Chem. Rev.*, 2012, **112**, 1105–1125.
4 A. H. Lu and F. Schüth, *Adv. Mater.*, 2006, **18**, 1793–1805.
5 (*a*) W. Chaikittisilp, M. Hu, H. Wang, H.-S. Huang, T. Fujita, K. C. W. Wu, L.-C. Chen, Y. Yamauchi and K. Ariga, *Chem. Commun.*, 2012, **48**, 7259–7261; (*b*) Y. H. Shih, C. P. Fu, W. L. Liu, C. H. Lin, H. Y. Huang and S. Ma, *Small*, 2016, **12**, 2057–2066.
6 A. Aijaz, N. Fujiwara and Q. Xu, *J. Am. Chem. Soc.*, 2014, **136**, 6790–6793.
7 L. Radhakrishnan, J. Reboul, S. Furukawa, P. Srinivasu, S. Kitagawa and Y. Yamauchi, *Chem. Mater.*, 2011, **23**, 1225–1231.
8 B. Liu, H. Shioyama, T. Akita and Q. Xu, *J. Am. Chem. Soc.*, 2008, **130**, 5390–5391.
9 (*a*) W. Xia, A. Mahmood, R. Zou and Q. Xu, *Energy Environ. Sci.*, 2015, **8**, 1837–1866; (*b*) L. Lux, K. Williams and S. Ma, *CrystEngComm*, 2015, **17**, 10–22.
10 P. D. C. Dietzel, B. Panella, M. Hirscher, R. Blom and H. Fjellvåg, *Chem. Commun.*, 2006, 959–961.
11 N. L. Rosi, J. Kim, M. Eddaoudi, B. Chen, M. O'Keeffe and O. M. Yaghi, *J. Am. Chem. Soc.*, 2005, **127**, 1504–1518.
12 S. R. Caskey, A. G. Wong-Foy and A. J. Matzger, *J. Am. Chem. Soc.*, 2008, **130**, 10870–10871.
13 S. Lim, K. Suh, Y. Kim, M. Yoon, H. Park, D. N. Dybtsev and K. Kim, *Chem. Commun.*, 2012, **48**, 7447–7449.
14 S. J. Yang, T. Kim, J. H. Im, Y. S. Kim, K. Lee, H. Jung and C. R. Park, *Chem. Mater.*, 2012, **24**, 464–470.
15 X. He, W. Zhong, C.-T. Au and Y. Du, *Nanoscale Res. Lett.*, 2013, **8**, 1.
16 J.-W. Jeon, R. Sharma, P. Meduri, B. W. Arey, H. T. Schaef, J. L. Lutkenhaus, J. P. Lemmon, P. K. Thallapally, M. I. Nandasiri, B. P. McGrail and S. K. Nune, *ACS Appl. Mater. Interfaces*, 2014, **6**, 7214–7222.
17 H.-L. Jiang, B. Liu, Y.-Q. Lan, K. Kuratani, T. Akita, H. Shioyama, F. Zong and Q. Xu, *J. Am. Chem. Soc.*, 2011, **133**, 11854–11857.
18 J. Chmiola, G. Yushin, Y. Gogotsi, C. Portet, P. Simon and P. L. Taberna, *Science*, 2006, **313**, 1760–1763.
19 Q. Lu, J. G. Chen and J. Q. Xiao, *Angew. Chem., Int. Ed.*, 2013, **52**, 1882–1889.

